Hindawi
Journal of Sensors
Volume 2022, Article ID 9928993, 12 pages
https://doi.org/10.1155/2022/9928993

Research Article

Superresolution Reconstruction Algorithm of Ultrasonic Logging Images Based on High-Frequency Enhancement

Ao Qiu,[1,2] Yibing Shi,[1] Xinyi Luo,[1] Zhipeng Li,[1] and Wei Zhang[1]

[1]*School of Automation Engineering, University of Electronic Science and Technology of China, 611731, China*
[2]*Welltech Research and Design Institute, China Oilfield Services Ltd., 065200, China*

Correspondence should be addressed to Wei Zhang; weizhang@uestc.edu.cn

Received 29 June 2022; Revised 27 October 2022; Accepted 29 October 2022; Published 21 November 2022

Academic Editor: Akhilesh Pathak

High-resolution logging images with glaring detail information are useful for analysing geological features in the field of ultrasonic logging. The resolution of logging images is, however, severely constrained by the complexity of the borehole and the frequency restriction of the ultrasonic transducer. In order to improve the image superresolution reconstruction algorithm, this paper proposes a type of ultrasonic logging based on high-frequency characteristics, with multiscale dilated convolution to feature as the basis of network-learning blocks, training in the fusion of different scale texture feature. The outcomes of other superresolution reconstruction algorithms are then compared to the outcomes of the two-, four-, and eightfold reconstruction. The proposed algorithm enhances subjective vision while also enhancing PSNR and SSIM evaluation indexes, according to a large number of experiments.

1. Introduction

Diverse sensing technologies are being applied to environment sensing or source exploration with the advancement of material technology [1–3]. By providing a crucial insight logging map with fracture and hole information to reflect the well's state, borehole imaging logging has grown to be a significant technology in the field of petroleum logging for oil exploration. The two primary logging techniques used in borehole imaging logging are circumference ultrasonic imaging and microresistivity scanning, with ultrasonic imaging being more widely used due to its high penetrability, high borehole coverage, and simple instrument structure. Figure 1 shows the principle of ultrasonic imaging logging. This instrument mainly uses ultrasonic transducer to send and receive ultrasonic signals in oil wells and adopts the principle of pulse reflection. Rotate the transducer while exciting the transducer to generate ultrasonic waves, so that it can rotate circumferentially downwards and emit scanning to the borehole wall; after the ultrasonic wave is transmitted, the reflected echo will be generated when it meets the borehole wall, and it will be returned to the transducer to be received. If the borehole diameter is different, the propagation time of ultrasonic wave in the borehole will be different, so the geometric image of the borehole wall can be inferred according to the propagation time of ultrasonic wave [4].

However, because of the influence of the downhole environment and hardware constraints, it is possible that the actual logging images obtained have low contrast and the detail information of the images may not be obvious [5], which makes it challenging to interpret the existing logging images and calls for image enhancement. Superresolution reconstruction is one of the most widely used processes for image enhancement. This method's objective is to generate a part with a certain degree of confidence while recovering a high-resolution image from a low-resolution part [6–8]. The research method is divided into interpolation-based reconstruction algorithms, such as the dual cubic interpolation method [9], which computes the weighted average of 16 known pixel points within the $4 * 4$ domain of the current pixel point. Many superresolution reconstruction techniques have been proposed in recent years [10, 11]. This interpolation method has a broad reconstruction effect but is simple to calculate. It also loses edge details. Li and Orchard proposed an edge-oriented natural image interpolation algorithm [12] to estimate the local covariance coefficients

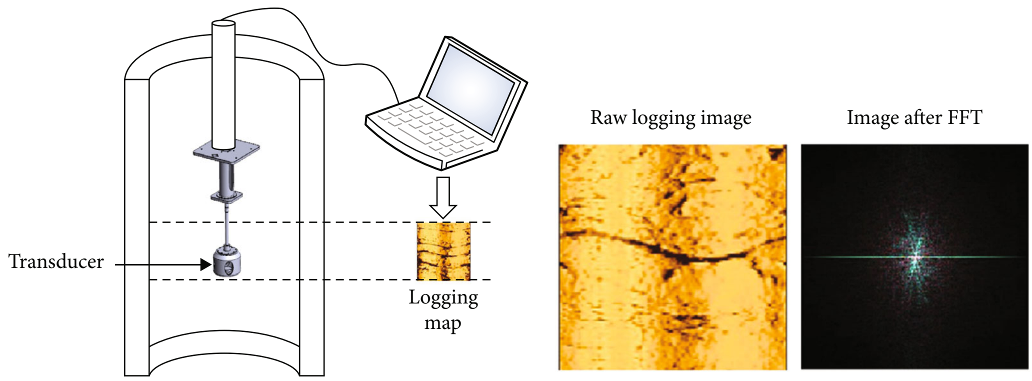

Figure 1: The principle of ultrasonic image logging. It is clear that raw logging images have numerous elements of high frequency.

from low-resolution images and derive higher-resolution images based on the covariance coefficients. Zhang and Wu proposed an edge-guided nonlinear interpolation method based on directional filtering and data fusion to obtain the pixels to be interpolated by linear minimum mean square error estimation [13]. Edge blurring is effectively suppressed by G. Cheng and L. Cheng's wavelet-based directional adaptive interpolation algorithm [14], which combines local directional adaptation with wavelet transform. Although the interpolation-based superresolution reconstruction method is simpler to compute, the image reconstruction effect is far from ideal because it lacks high-level image features [15]. More and more people are researching learning-based reconstruction algorithms because they can learn from a lot of image data and create a suitable network model to enhance the reconstruction effect. The SRCNN was proposed by Dong et al. [16] and uses dual triple interpolation to perform upsampling before using deep learning to reconstruct images using a three-layer neural network. When compared to the conventional interpolation method, the image reconstruction effect is significantly improved. The residual network [17] used as a reference in VDSR [18], which was developed by Kim et al., can prevent gradient disappearance and enhance network training stability in addition to deepening the network structure.

Inverse convolution is used for upsampling, and a small convolution kernel is used in place of the large convolution kernel in FSRCNN [19], which enhances the SRCNN model. In order to preserve as much feature information as possible and enhance the reconstruction effect, Shi et al. proposed the ESPCN [20] method, which can perform feature extraction directly on low-resolution images and then upsample using subpixel convolution. Ledig et al.'s [21] proposed SRResNet and SRGAN, which introduced generative adversarial networks, to enhance the visual effect. The EBRN networks proposed by Qiu [22] suggest that the complexity of low-frequency and high-frequency information in images varies, and that low-frequency information is recovered with simple networks to avoid overfitting while high-frequency information is recovered with complex networks to avoid underfitting.

The aforementioned algorithms also suffer from flaws like insufficient high-frequency feature reconstruction, ineffective feature correlation, and insufficient feature acquisition. However, unlike other optical images, raw logging images created by ultrasonic waves only have a single channel and contain a significant amount of high-frequency data, as shown in Figure 1.

In light of this, this paper suggests an ultrasonic logging image superresolution reconstruction algorithm based on high-frequency feature enhancement. The network is first fed with the low-resolution image, and after a predetermined number of layers, the multiscale dilated convolution block mapping high-level feature is applied. Upsampling and downsampling are then applied, and the low-resolution image and the resulting results are compared to derive the unlearned high-frequency information. The original results are kept while the high-frequency data is fed into a different multiscale dilated convolution block for strengthening training. The enhanced training of high-frequency information is then repeated several times after the results of the high-frequency information training are combined with the initial results. The proposed method can effectively improve the reconstruction effect in terms of both objective index and subjective vision when compared to the classical hypersegmentation models of SRCNN, VDSR, SRResNet, and SRGAN.

The main innovations and contributions of this paper include the following: (1) proposing a multiscale dilated convolution block that uses dilated convolution to build convolution kernels of various sizes, fully acquiring the scale features of various perceptual fields of the image and fusing them to make the features more global.

(2) In the high-level feature mapping, the high-frequency feature enhancement structure is designed to compare with the original image several times in order to find unlearned high-frequency features and improve learning. All math symbols existing in the paper are defined as in Table 1.

2. Related Work

Deep learning (DL) has developed greatly with computers developing over the last decade, which has remarkably promoted the development of information technology in various fields [23–25]. Scientists reconstructed DL frameworks and proposed some revolutionary techniques such

Table 1: Math symbols in the paper.

I_{LR}	Low-resolution image
I_{HR}	Original high-resolution image
F_0	Feature extraction layer function
OUT_0	Output of the first layer
F_i	Function of multiscale dilated convolution block at stage i
LR_{HF1}	Missing high-frequency information after the first stage training
F_T	Transform of upsampling, downsampling, and converting to three-channel images
F_{HFi}	Function of multiscale dilated convolution residual block at stage i
HF_i	High-level feature of high-frequency information at stage i
OUT_i	High-level feature obtained at stage i
K_i	Convolution kernel size after expansion, $i \in [1, 3]$
H	Function of upsampling and generating a three-channel image
out_{i-1}	Output of the $i-1$ layer
F_{ki}	Convolutional layer function of the $3*3$ convolution kernel with expansion rate i, $i \in [1, 3]$
F_{1*1}	Convolutional layer function of the $1*1$ convolution kernel
out_{out}	Output of feature fusion
out_i	Output of the i multiscale dilated convolution residual block
BN	Batch normalization
PReLU	Parametric rectified linear unit

as convolutional neural network (CNN) [26], recurrent neural network (RNN) [23], or generative adversarial network (GAN) [27, 28]. During these techniques, dilated convolution and residual network are representatives that can improve performances of models in forward and backward phases when training.

2.1. Dilated Convolution. When the convolution kernel processes the data, the dilated convolution [29] layer adds a new "dilation" coefficient that establishes the value spacing. The same amount of computation will produce a $5*5$ receptive field with the same number of parameters as the $3*3$ convolution kernel if the normal convolution kernel is assumed to be $3*3$, 2 dilation rates, and the input. In the papers [30, 31] and others, dilated convolution was introduced to obtain a wider range of feature information and capture richer detailed features, all with predictable outcomes.

2.2. Residual Network. The problem of gradient disappearance and gradient explosion while training a deep network was addressed by He et al. in 2015 when they proposed a residual network that uses a skip connection to transfer information from the earlier convolutional layer directly to the later convolutional layer, allowing the original input to be transferred directly to the output. The residual network, which sped up network convergence and significantly reduced the issue of model overfitting for better deep-level network training, was introduced and improved in the papers [32–37].

3. Proposed Method

3.1. Network. In this paper, a multiscale dilated convolutional residual network with enhanced high-frequency features is proposed as shown in Figure 2. Suppose the input image be the low-resolution image I_{LR} after double-triple interpolation of the original high resolution I_{HR}, and the low-level features are extracted by the shallow feature extraction layer of the low-resolution image reconstruction network, which is expressed by the following equation:

$$OUT_0 = F_0(I_{LR}), \tag{1}$$

where F_0 is the shallow feature extraction layer function and OUT_0 represents the output of this layer. Then, input to four multiscale dilated convolution blocks for high-level feature extraction to get the result OUT_1, upsampling and downsampling in turn. Then, compare the output low frequency information I_{LR} and OUT_1 to get high-frequency information LR_{HF1}; input LR_{HF1} to four multiscale dilated convolution blocks separately for enhanced training to get HF_1; continue to input OUT_1 to four multiscale dilated convolution residual blocks to get high-level feature OUT_2. These can be expressed by the following equation:

$$\begin{aligned} OUT_1 &= F_1(OUT_0), \\ LR_{HF1} &= I_{LR} - F_T(OUT_1), \\ HF_1 &= F_{HF1}(LR_{HF1}), \\ OUT_2 &= F_2(OUT_1) + HF_1, \end{aligned} \tag{2}$$

where F_i is the function of multiscale dilated convolution block at stage i, $i \in [1, 4]$, LR_{HF1} is the missing high-frequency information after the first stage training, F_T is the function that has been upsampled, downsampled, and converted to three-channel images, F_{HF1} is the function of multiscale dilated convolution residual block used for high-frequency information enhancement, HF_1 is the high-level feature of high-frequency information, and OUT_i is the high-level feature obtained at stage i. The specific structure of the multiscale dilated convolution block will be discussed in Section 3.2. The above process is repeated to obtain high-frequency information several times to enhance the reconstruction of logging images:

$$\begin{aligned} HF_2 &= F_{HF2}(I_{LR} - F_T(F_2(OUT_2))), \\ OUT_3 &= F_3(OUT_2) + HF_2, \\ HF_3 &= F_{HF3}(I_{LR} - F_T(F_3(OUT_3))), \end{aligned}$$

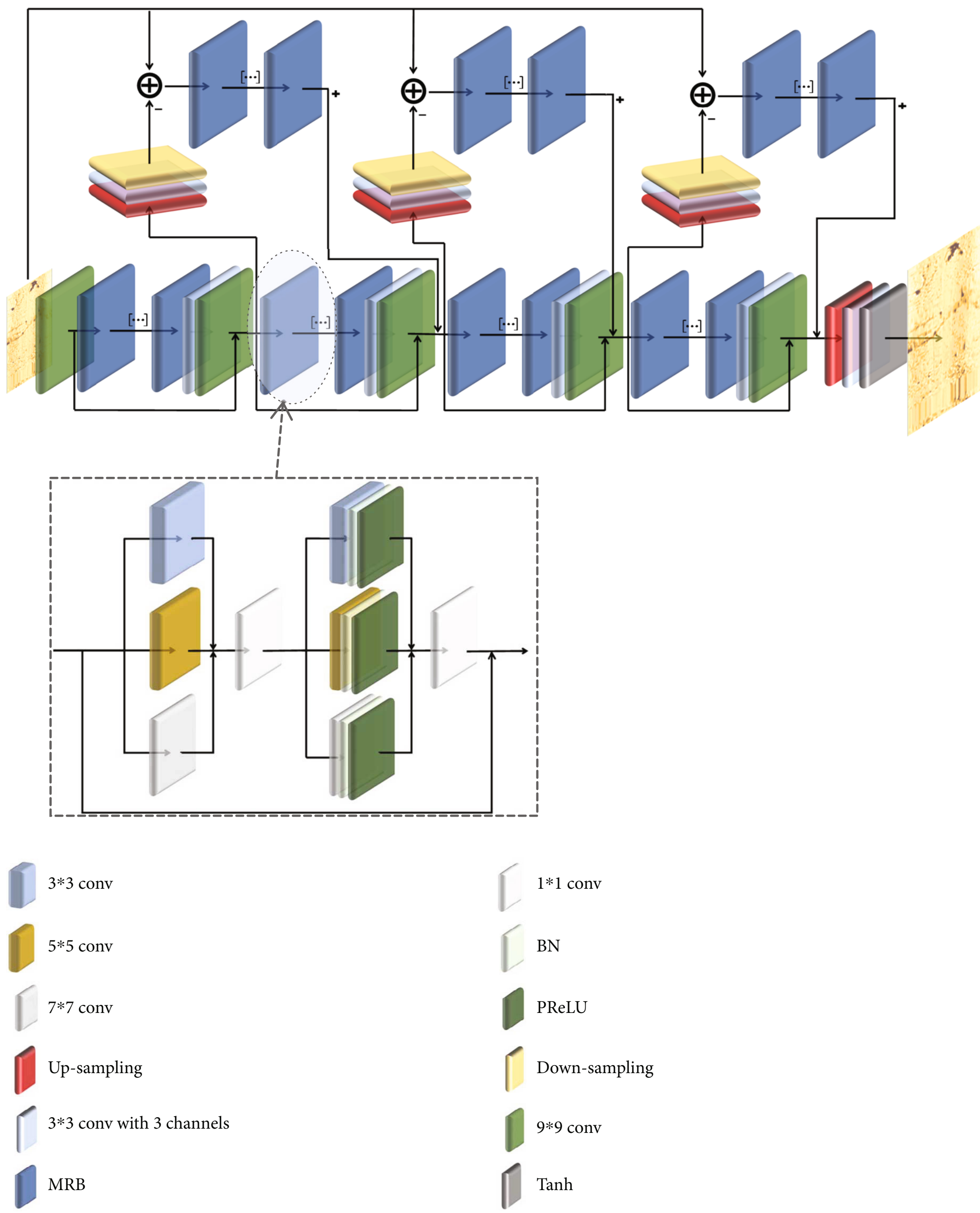

Figure 2: Our networks: the superresolution reconstruction algorithm based on high-frequency feature enhancement is based on multiscale dilated convolution blocks.

$$\begin{aligned}\mathrm{OUT} &= \mathrm{OUT}_3 + \mathrm{HF}_3 \\ &= \mathrm{OUT}_2 + \mathrm{HF}_2 + \mathrm{HF}_3 \\ &= \mathrm{OUT}_1 + \mathrm{HF}_1 + \mathrm{HF}_2 + \mathrm{HF}_3.\end{aligned} \tag{3}$$

OUT is upsampled by a subpixel convolutional layer to obtain a three-channel reconstructed image SR_L, as shown in the following equation.

$$\mathrm{SR}_L = H(\mathrm{OUT}), \tag{4}$$

where H is a function of upsampling and generating a three-channel image.

3.2. Multiscale Dilated Convolution Blocks. Convolution kernels of various sizes can be used to obtain features of various scales, and the features obtained by combining these features are often superior to those obtained by a single scale [38–41]. The yellow arrow in Figure 2 shows the multiscale dilated convolution block (MRB) designed in this paper, which adopts a convolution kernel of size $3 * 3$ on which the dilated convolution with a dilation rate of 2 and a dilation rate of 3 is used to obtain receptive fields of $5 * 5$ and $7 * 7$ convolution kernel sizes, respectively, as shown in Figure 3, which is centered on the red number 3. And the grid occupied by 3 indicates the range of features extracted by the convolution kernel of size $3 * 3$ and the grid occupied by 5. The feature range extracted by $3 * 3$ convolutional kernel with expansion factor of 2 is represented by grid 3, and the feature range extracted by $3 * 3$ convolutional kernel with the expansion factor of 3 is represented by grid 7.

The computation does not increase the computational effort because the expansion is done with 0 as shown in the following equation:

$$
\begin{aligned}
K_1 &= k + (k-1)(r-1) = 3, \\
K_2 &= k + (k-1)(r-1) = 5, \\
K_3 &= k + (k-1)(r-1) = 7,
\end{aligned}
\tag{5}
$$

where k is the convolution kernel size, r is the expansion coefficient, and K_i is the convolution kernel size after expansion, $i \in [1, 3]$.

The output results of three different convolutional kernel sizes are summed and input again into these three convolutional kernels, and a $1 * 1$ size convolutional kernel is used for feature fusion, and finally, the feature fusion and input results are summed to establish a residual structure that facilitates network convergence, as shown in the equation below:

$$
\begin{aligned}
\mathrm{out}_{11} &= F_{k1}(\mathrm{out}_{i-1}), \\
\mathrm{out}_{12} &= F_{k2}(\mathrm{out}_{i-1}), \\
\mathrm{out}_{13} &= F_{k3}(\mathrm{out}_{i-1}), \\
\mathrm{out} &= \mathrm{torch.cat}(\mathrm{out}_{11} + \mathrm{out}_{12} + \mathrm{out}_{13}), \\
\mathrm{out}_{21} &= F_{k1}(\mathrm{out}), \\
\mathrm{out}_{22} &= F_{k2}(\mathrm{out}), \\
\mathrm{out}_{23} &= F_{k3}(\mathrm{out}), \\
\mathrm{out}_{\mathrm{out}} &= \mathrm{PRelu}(\mathrm{BN}(F_{1*1}(\mathrm{out}_{21}, \mathrm{out}_{22}, \mathrm{out}_{23}))), \\
\mathrm{out}_i &= \mathrm{out}_{\mathrm{out}} + \mathrm{out}_{i-1},
\end{aligned}
\tag{6}
$$

where out_{i-1} is the output of the $i-1$ layer, F_{ki} is the convolutional layer function of the $3 * 3$ convolution kernel with expansion rate i, $i \in [1, 3]$, F_{1*1} is the convolutional layer function of the $1 * 1$ convolution kernel, $\mathrm{out}_{\mathrm{out}}$ is the output of feature fusion, and out_i is the output of the i multiscale dilated convolution residual block.

4. Experiments

4.1. Experiment Setups. As shown in Figure 4, we created a unique imaging logging tool that consists of a downhole logging device and a ground control system. The computer and power supply that are part of the ground control system are intended to let ground engineers control the transmission and reception of ultrasonic signals as well as the creation of images of borehole walls. A downhole logging device is used to transmit bipolar pulses to drive the transducer while simultaneously gathering and processing ultrasonic signals reflected from strata at various depths. An armored cluster cable that connects the two pieces acts as a conduit for power and communication between the surface and the underground. The field-programmable gate array (FPGA) on the main control circuit board first receives the order during a signal processing cycle. It then sends a bipolar pulse to the drive circuit, which causes the piezoelectric ceramic to generate ultrasonic waves. The same piezoelectric ceramic will pick up the signals reflected off the borehole walls and transmit them to the main control circuit board using an analog-to-digital converter (ADC) with a 20 MHz sampling rate. All of the acquisition circuit's hardware filters are present. The time of flight (ToF), amplitude, and other ancillary data of echo signals are then calculated using the preset algorithm using the same FPGA. These data are kept in a large-capacity NAND flash and sent to the ground control system by the downhole instrument bus of the enhancing logging image system (EDIB). Finally, using data from the main control circuit board, the ground system can visualize strata at various depths by creating borehole walls based on ToF and echo signal amplitudes that correspond to the various strata's positions. The ground system's host display software is in charge of combining logging images and interaction with instructions. In this paper, the training and test sets are sequentially derived from the circumference ultrasonic logging tool data acquired in the field in Zhanjiang. The echoes are gathered underground and transmitted to the surface control system via the EDIB bus. The surface computer receives the data via a USB port, extracts the echo's amplitude and arrival time, and then synthesizes the final logging images, of which 1462 images are used as the training set and 589 images as the test set.

The local hardware environment used for the experiments is a laptop with a 64-bit Windows 10-based operating system and an AMD Ryzen 5 3550H CPU. Computational acceleration was performed using Colaboratory, a cloud-based environment provided by Google, with 16G of video memory.

The specific training process is as follows:

(1) Initialize the network parameters and set 64 images as a batch, and the learning rate is 0.0001

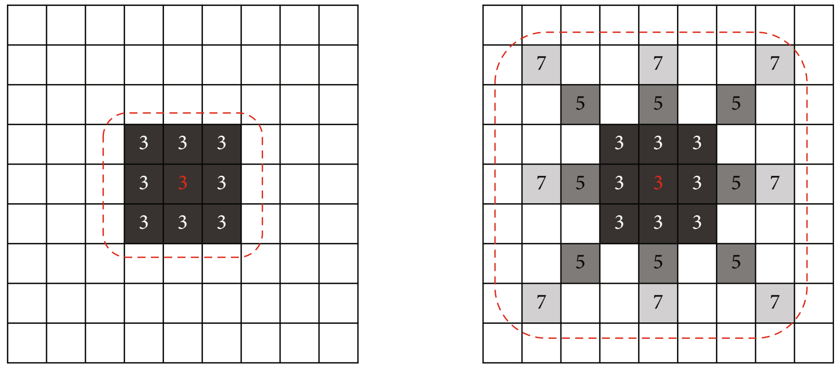

Figure 3: Diagram of receptive field by multiscale dilated convolution block.

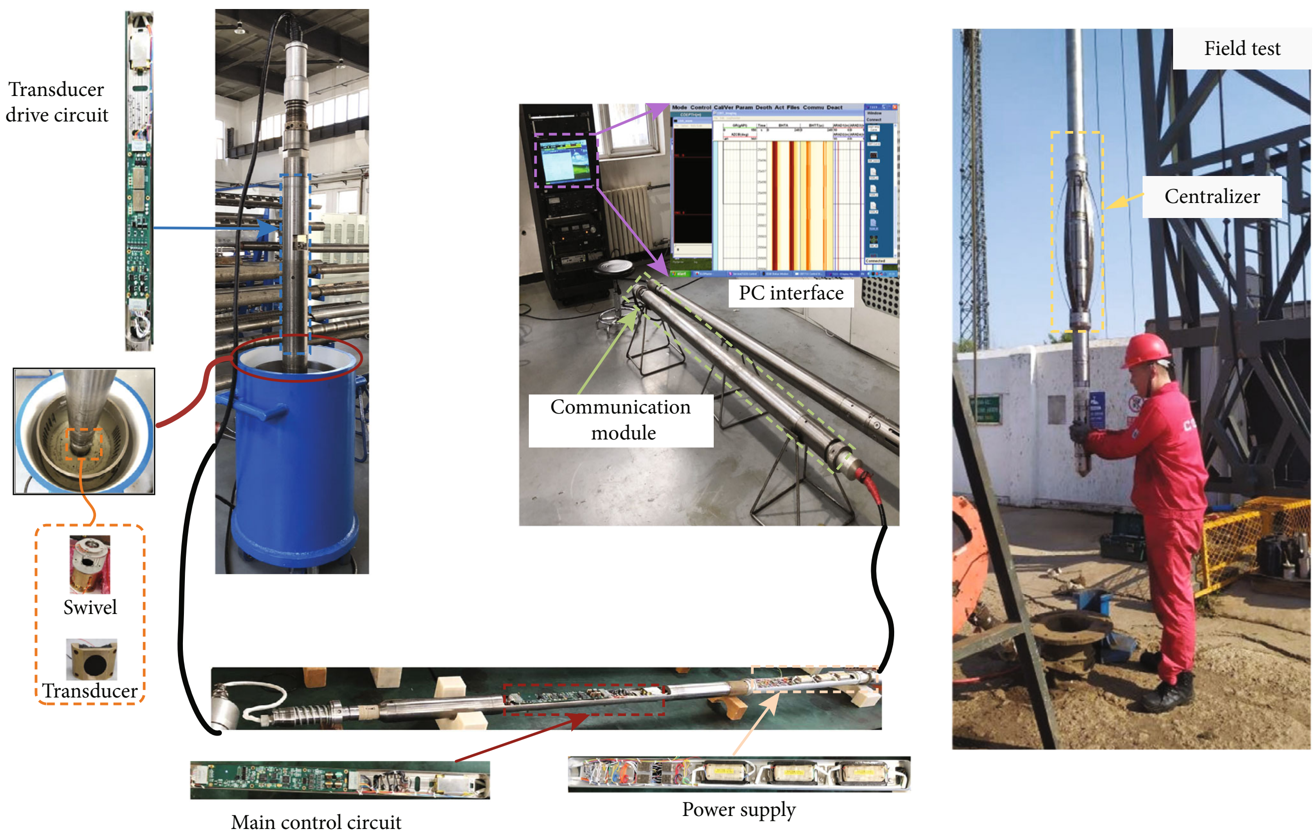

Figure 4: Logging operation in Zhanjiang.

(2) Input I_{HR} and four times downsampling using bitriple interpolation to obtain I_{LR}

(3) Input I_{LR} to the network; after the first segment of the residual network composed of four multiscale dilated convolution blocks, get OUT_1; the results of I_{LR} and OUT_1 are differenced by upsampling and downsampling in turn to get high-frequency information LR_{HF1}; in order to strengthen the training of high-frequency information, LR_{HF1} is input to the residual network composed of four multiscale dilated convolution blocks. Obtain the high-level feature HF_1 and sum up HF_1 and OUT_1 as the input of the second residual network

(4) Repeat step (3) to get the second stage result OUT_2 and enhanced high-frequency information HF_2, respectively, and take them as the input of the third segment of the residual network; repeat step (3) again to get the third stage result OUT_3 and enhanced high-frequency information HF_3, then take them as the input of the fourth segment of the residual network to get the result OUT_4.

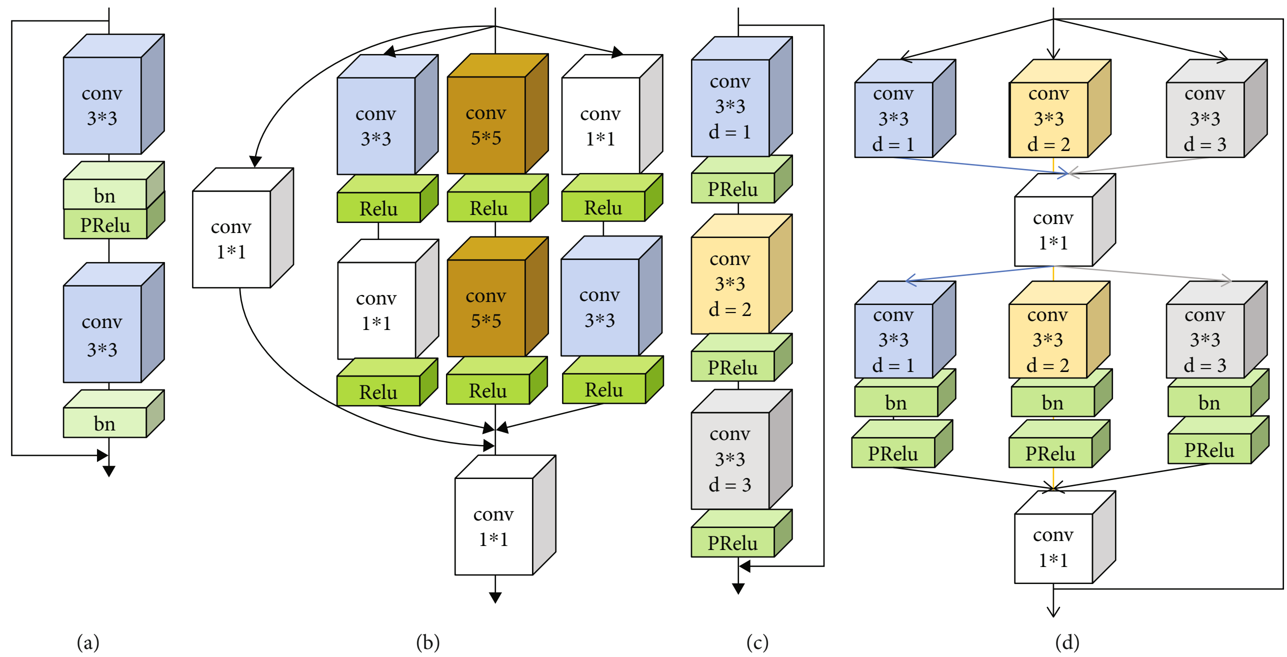

FIGURE 5: Multiscale feature extraction structure: (a) is the single-scale SRResNet base block, (b) the modified structure of inception V1 base block for multiscale structure, (c) is the multiscale structure proposed in paper [18], and (d) is the multiscale structure proposed in this paper.

(5) Upsample and reconstruct OUT_4 to get three-channel reconstructed image SR_L.

(6) Calculate $L1$ loss function from SR_L and the original high-resolution image I_{HR} to obtain L_{LR} and use the Adam optimization algorithm to update the parameters of the low-resolution image reconstruction network

(7) Based on the results of L_{HR}, the network is updated with parameters using the Adam optimization algorithm

(8) After 200 iterations, the trained network model is obtained, and the images of the test set are tested directly in the low-resolution image reconstruction network

In this paper, we use peak signal-to-noise ratio (PSNR) and structural similarity (SSIM), which are common evaluation metrics in the field of image hypersegmentation [42–44]; to compare the reconstruction effect, PSNR is used to describe the distortion caused by random noise on the reconstructed image as shown in the following equation.

$$\mathrm{PSNR} = 10\log_{10}\frac{(2^n-1)^2}{\mathrm{MSE}}, \tag{7}$$

where n is the number of bits per pixel, generally taken as 8, and MSE is the mean square error.

SSIM is a comparison of two images in terms of contrast, structural features and brightness; the higher the PSNR the less distortion, and the higher the SSIM the closer the image is.

$$\begin{aligned} l(X,Y) &= \frac{2\mu_X\mu_Y + C_1}{\mu_X{}^2 + \mu_Y{}^2 + C_1}, \\ c(X,Y) &= \frac{2\sigma_X\sigma_Y + C_2}{\sigma_X{}^2 + \sigma_Y{}^2 + C_2}, \\ s(X,Y) &= \frac{\sigma_{XY} + C_3}{\sigma_X\sigma_Y + C_3}, \\ \mathrm{SSIM}(X,Y) &= l(X,Y)\bullet c(X,Y)\bullet s(X,Y). \end{aligned} \tag{8}$$

Among them, μ_X and μ_Y represent the mean values of image SR and image HR, respectively; σ_X and σ_Y represent the standard deviation of image SR and HR, respectively; $\sigma_X{}^2$ and $\sigma_Y{}^2$ represent the variance of image SR and HR, respectively. σ_{XY} represents the image SR and HR covariance and C_1, C_2, and C_3 are constants.

4.2. Experiment Analysis. In order to verify the merits of the algorithm proposed in this paper, the structure of this paper is verified step by step.

4.2.1. Ablation Study: Effect of Multiscale Dilated Convolution Blocks on the Results. The structures in Figure 5 are compared in this subsection to show the efficacy of the proposed multiscale dilated convolution block for feature extraction in this paper, where the latter three structures are used for multiscale feature extraction. Figure 5(a) depicts the SRResNet base block, Figure 5(b) depicts the modified

Table 2: The reconstruction effect of multiscale dilated convolution block.

Magnification	Metrics	(a)	(b)	(c)	(d)
$\times 2$	PSNR	36.462	35.980	35.830	**36.496**
	SSIM	0.963	0.959	0.956	**0.961**
	Parameters	1401 k	4672 k	1981 k	**7505** k
$\times 4$	PSNR	30.990	30.895	30.716	**31.126**
	SSIM	0.858	0.857	0.857	**0.860**
	Parameters	1542 k	4812 k	2131 k	**7653** k
$\times 8$	PSNR/dB	27.325	27.172	26.767	**27.355**
	SSIM	0.714	0.716	0.700	**0.718**
	Parameters	1691 k	7262 k	2283 k	**9713** k

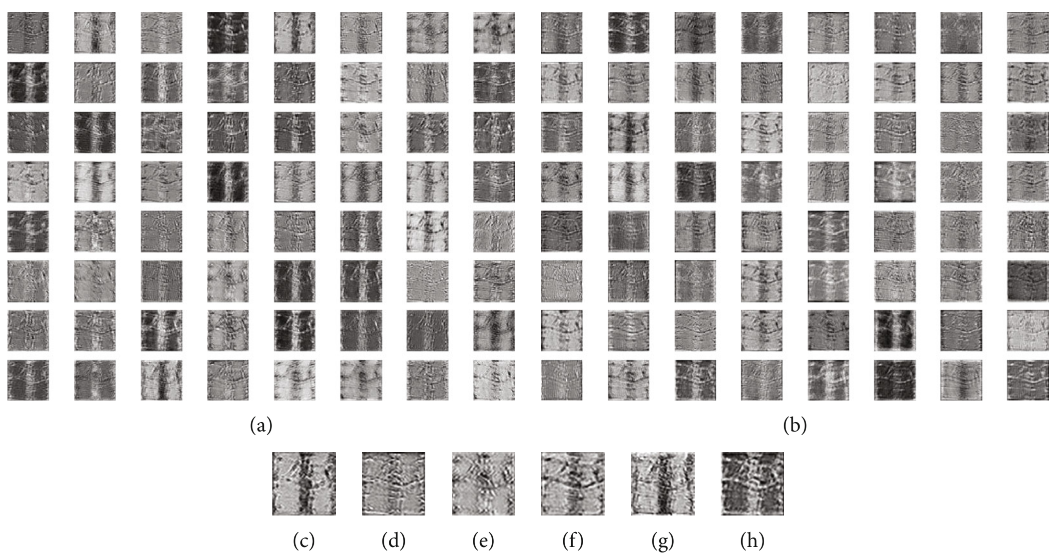

Figure 6: Feature map comparison: (a) is the 64-channel feature map extracted from the 16th residual block of SRResNet; (c), (e), and (g) are the amplification display of the feature map of the 4th, 42nd, and 58th channels, respectively; (b) is the 64-channel feature map extracted from the 16th block of the multiscale cavity convolution block proposed in this paper; and (d), (f), and (h) are the enlarged display of the feature map of the 4th, 42nd, and 58th channels, respectively.

structure modeled after the inception V1 base block, Figure 5(c) depicts the dilated convolution base block, and Figure 5(d) depicts the multiscale dilated convolution block proposed in this paper. The results of doing 2 times, 4 times, and 8 times of reconstruction are shown in Table 2, with the number of all five base blocks in Figures 5(a)–5(d) being 16 and the rest of the modules and parameter settings being identical.

From the above results, we can see that in the 2 times, 4 times, and 8 times magnification, the single-scale feature acquisition structure in Figure 5(a) is significantly worse than the remaining three multiscale feature acquisition structures, whereas the proposed Figure 5(d) structure in this paper has the best metrics, with about 0.136 improvement in PSNR and 0.002 improvement in SSIM when compared to the single-scale under 4 times of reconstruction.

The feature maps Figure 6(a) of the residual block through SRResNet and the feature maps Figure 6(b) of the multiscale dilated convolution block are compared in Figure 6 to better understand the proposed multiscale dilated convolution block in this paper. Figures 6(d), 6(f), and 6(h) are feature maps of the multiscale dilated convolution block through the scale dilated convolution block of the 4th, 42nd, and 58th channels, respectively, and Figures 6(c), 6(e), and 6(g) are feature maps of the 4th, 42nd, and 58th channels through the residual block of SRResNet, respectively. The proposed structure in this paper obtains more comprehensive features and clearer textures, as can be seen.

4.2.2. Impact of High-Frequency Feature Enhancement. Table 3 shows the comparative effects of objective metrics after reconstruction of SRResNet (a in the table), SRResNet-based primary high-frequency feature-enhanced structure (b in the table), and SRResNet-based four high-frequency feature-enhanced structure (c in the table) with the effect of $\times 2$ and $\times 4$ magnification. a, b, and c structures in Table 3 have the same residual block structure and

Table 3: The reconstruction effect of Parallel structure.

Magnification	Specification	a	b	c
× 2	PSNR	36.462	36.692	**36.800**
	SSIM	0.963	0.962	**0.962**
	Parameters	1401749	2328870	**3188406**
× 4	PSNR	30.990	30.682	**31.247**
	SSIM	0.858	0.849	**0.859**
	Parameters	1549462	2820904	**4369082**

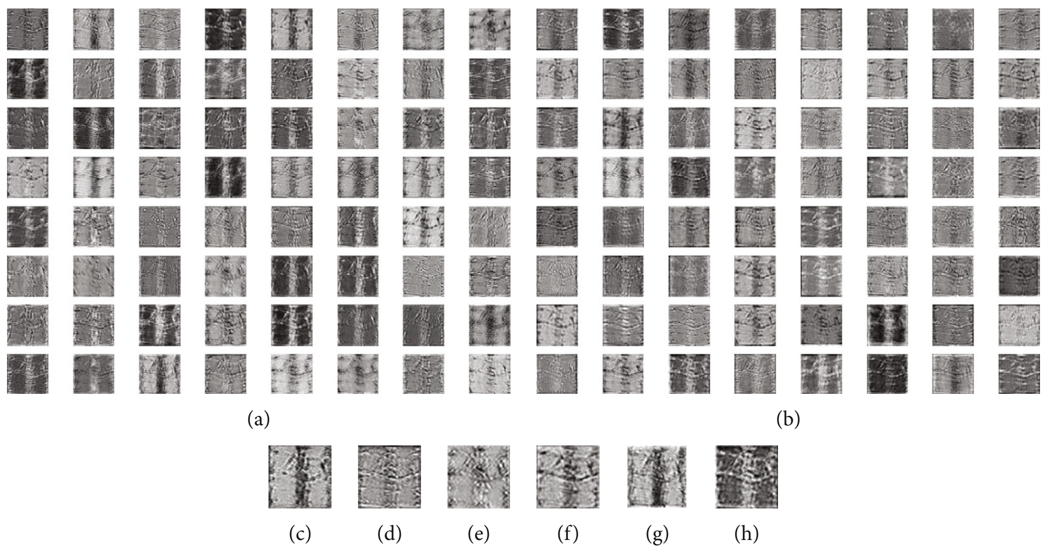

Figure 7: Feature map comparison: (a) is the 64-channel feature map extracted from the 16th residual block of SRResNet; (c), (e), and (g) are the amplification display of the feature map of the 4th, 42nd, and 55th channels, respectively; (b) is the 64-channel feature map extracted from the 16th block of the multiscale cavity convolution block proposed in this paper; and (d), (f), and (h) are the enlarged display of the feature map of the 4th, 42nd, and 55th channels, respectively.

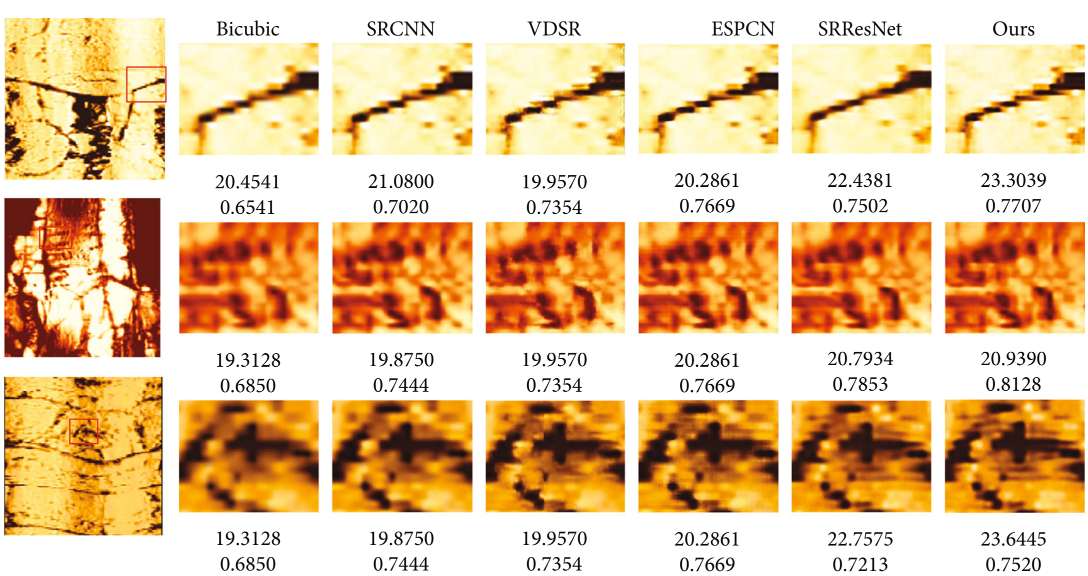

Figure 8: The reconstruction effect of single log image.

Table 4: The reconstruction effect of our method and others.

Magnification	Specification	SRCNN	VDSR	SRResNet	Ours
× 2	PSNR	35.233	36.398	36.462	37.981
	SSIM	0.935	0.951	0.963	0.973
	Parameters	8129	664707	1401749	15188965
× 4	PSNR	29.833	30.831	30.990	31.425
	SSIM	0.864	0.830	0.858	0.867
	Parameters	8129	664707	1549462	15336678

number, and the remaining parameter settings are exactly the same.

We can obtain the unlearned high-frequency detail information by comparing the reconstruction effect of the mapped high-level features with the original low-resolution image using the above experiments, and it is effective to do strengthening learning of this high-frequency detail information alone and repeat this process several times. Under fourfold reconstruction, the PSNR improves by 0.257 and the SSIM improves by about 0.001.

The feature maps of low-resolution images with direct feature learning Figure 7(a) and enhanced high-frequency feature training Figure 7(b) are compared in Figure 7, where Figures 7(c), 7(e), and 7(g) are the feature maps of the 4th, 42nd, and 55th channels through SRResNet residual blocks, respectively, and Figures 7(d), 7(f), and 7(h) are the feature maps of the 4th, 42nd, and 55th channels after high-frequency feature enhancement proposed in this paper.

4.2.3. Comparison of the Method in This Paper with Others. The multiple average PSNR and average SSIM values of this algorithm and other hypersegmentation algorithms in the test set for single image reconstruction tests are shown in Figure 8 and Table 4.

The PSNR and SSIM metrics, as well as the number of model parameters, are compared in Table 4 between this method and other classical hypersegmentation methods. On a single log image, Figure 8 shows the reconstruction results as well as a comparison of PSNR and SSIM metrics between this method and other classical hypersegmentation methods. The method has significantly improved the metrics when compared to traditional methods and other classical deep learning methods, with PSNR of more than 0.435 and SSIM of more than 0.009, and the subjective visual effect has also been improved, with clearer and more accurate edges, as shown in the figure.

5. Conclusion

In this paper, a high-frequency feature-enhanced superresolution reconstruction method for logging images is proposed as a solution to the problem of feature extraction being insufficiently thorough and detail information not being learned in depth. The algorithm uses multiscale dilated convolution blocks to extract various feature information, and the dilated convolution expands the receptive field without adding more parameters. As a result of the method's repeated extraction of high-frequency features, detail information that was not learned during reconstruction can be learned and improved. The circumference ultrasonic logging tool's real logging images are used as the training set to assess the method's efficacy. The reconstructed images are evaluated using the PSNR and SSIM image quality evaluation criteria. The experimental results show that the method described in this paper can recover better high-resolution images and extract more feature information. Lightweight networks will be the primary area of research for future optimization.

Data Availability

The data used to support the findings of this study are available from the corresponding author upon request.

Conflicts of Interest

The authors declare that they have no conflict of interest.

Acknowledgments

The research is supported by the Development and Industrial Application of Ultra-High Temperature and High-Pressure Wireline Logging System from Science and Technology Project of China National Offshore Oil Corporation under the Grant numbered CNOOC-KJ ZDHXJSGG YF 2019-02.

References

[1] M. Li, R. Singh, M. S. Soares, C. Marques, B. Zhang, and S. Kumar, "Convex fiber-tapered seven core fiber-convex fiber (CTC) structure-based biosensor for creatinine detection in aquaculture," *Optics Express*, vol. 30, no. 8, pp. 13898–13914, 2022.

[2] Y. Wang, G. Zhu, M. Li et al., "Water pollutants p-cresol detection based on au-ZnO nanoparticles modified tapered optical fiber," *IEEE Transactions on Nanobioscience*, vol. 20, no. 3, pp. 377–384, 2021.

[3] S. Kumar, Z. Guo, R. Singh et al., "MoS2functionalized multicore fiber probes for selective detection ofShigellabacteria based on localized plasmon," *Journal of Lightwave Technology*, vol. 39, no. 12, pp. 4069–4081, 2021.

[4] Z. Li, T. Wu, W. Zhang et al., "A study on determining time-of-flight difference of overlapping ultrasonic signal: wave-transform network," *Sensors*, vol. 20, no. 18, p. 5140, 2020.

[5] F. Qingqing, *Research on Ultrasonic Imaging Logging Image Enhancement and Recovery Method, [Ph.D. Thesis]*, Changjiang University, 2020.

[6] Z. Dengwen, Z. Lijuan, D. Ran, and C. Xiaoliang, "Image super-resolution reconstruction based on recursive residual network," *Journal of Automation*, vol. 45, no. 6, pp. 1157–1165, 2019.

[7] C. Ma, Y. Guo, P. Wu, and H. Liu, "A review of image enhancement research in generative adversarial networks," *Information Network Security*, vol. 5, pp. 10–21, 2019.

[8] W. Wanliang, Y. Xiaohan, Z. Yanwei, G. Nan, L. Chong, and Z. Zhaojuan, "Image enhancement algorithm using convolutional self-encoder network," *Journal of Zhejiang University (Engineering Edition)*, vol. 53, no. 9, pp. 1728–1740, 2019.

[9] R. Keys, "Cubic convolution interpolation for digital image processing," *IEEE Transactions on Acoustics, Speech, and Signal Processing*, vol. 29, no. 6, pp. 1153–1160, 1981.

[10] L. Zhong Baojiang and J. J. Zhifang, "A review of image interpolation techniques," *Data Acquisition and Processing*, vol. 31, no. 6, pp. 1083–1096, 2016.

[11] J. Zou, Z. Li, Z. Guo, and D. Hong, "Super-resolution reconstruction of images based on microarray camera," *Computers, Materials & Continua*, vol. 60, no. 1, pp. 163–177, 2019.

[12] X. Li and M. T. Orchard, "New edge-directed interpolation," *IEEE Transactions on Image Processing*, vol. 10, no. 10, pp. 1521–1527, 2001.

[13] L. Zhang and X. Wu, "An edge-guided image interpolation algorithm via directional filtering and data fusion," *IEEE Transactions on Image Processing*, vol. 15, no. 8, pp. 2226–2238, 2006.

[14] G. Cheng and L. Cheng, "Wavelet-based directional adaptive image interpolation," *Journal of Electronics and Information*, vol. 31, no. 2, pp. 265–269, 2009.

[15] W.-W. Chen, *Research and Implementation of Image Super-Resolution Reconstruction Algorithm, [Ph.D. Thesis]*, University of Electronic Science and Technology, 2020.

[16] C. Dong, C. C. Loy, K. He, and X. Tang, "Learning a deep convolutional network for image super-resolution," in *European Conference on Computer Vision (ECCV)*, pp. 184–199, Berlin, Germany, 2014.

[17] K. He, X. Zhang, S. Ren, and J. Sun, "Deep residual learning for image recognition," in *Proceedings of 2016 IEEE Conference on Computer Vision and Pattern Recognition*, pp. 770–778, Las Vegas, NV, USA, 2016.

[18] J. Kim, J. K. Lee, and K. M. Lee, "Accurate image super resolution using very deep convolutional networks," in *Proceedings of 2016 EEE Conference on Computer Vision and Pattern Recognition*, Las Vegas, NV, USA, 2016.

[19] C. Dong, C. L. Chen, and X. Tang, "Accelerating the super-resolution convolutional neural network," in *European Conference On Computer Vision*, Springer, 2016.

[20] W. Shi, J. Caballero, F. Huszár et al., "Real-time single image and video super-resolution using an efficient sub-pixel convolutional neural network," in *Proceedings of 2016 IEEE Conference on Computer Vision and Pattern Recognition*, pp. 1874–1883, Las Vegas, NV, USA, 2016.

[21] C. Ledig, L. Theis, F. Huszár et al., "Photo-realistic single image super-resolution using a generative adversarial network," in *Proceedings of the IEEE conference on computer vision and pattern recognition (CVPR)*, pp. 105–114, Hawaii, USA, 2017.

[22] Q. Yajun, *Research on Super-Resolution Reconstruction Algorithm Based on Deep Learning, [Ph.D. Thesis]*, Yunnan University, 2020.

[23] J. Wang, Y. Zou, P. Lei, R. S. Sherratt, and L. Wang, "Research on recurrent neural network based crack opening prediction of concrete dam," *Journal of Internet Technology*, vol. 21, no. 4, pp. 1151–1160, 2020.

[24] P. Bin, K. Li, S. Li, and N. Zhu, "Automatic fetal ultrasound standard plane recognition based on deep learning and IIoT," *IEEE Transactions on Industrial Informatics*, vol. 17, no. 11, pp. 7771–7780, 2021.

[25] J. Zhang, S. Zhong, T. Wang, H.-C. Chao, and J. Wang, "Blockchain-based systems and applications: a survey," *Journal of Internet Technology*, vol. 21, no. 1, pp. 1–14, 2020.

[26] S. Zhou and J. Qiu, "Enhanced SSD with interactive multi-scale attention features for object detection," *Multimedia Tools and Applications*, vol. 80, no. 8, pp. 11539–11556, 2021.

[27] M. Zhao, X. Liu, X. Yao, and K. He, "Better visual image super-resolution with laplacian pyramid of generative adversarial networks," *Computers, Materials & Continua*, vol. 64, no. 3, pp. 1601–1614, 2020.

[28] H. Ke, P. Li, S. Guo, and M. Guo, "On traffic-aware partition and aggregation in MapReduce for big data applications," *IEEE Transactions on Parallel and Distributed Systems*, vol. 27, no. 3, pp. 818–828, 2016.

[29] C. L. Zhang, J. W. Zhao, and F. L. Cao, "Construction of deep neural network with null convolution for reconstructing high-resolution images," *Pattern Recognition and Artificial Intelligence*, vol. 32, no. 3, pp. 259–267, 2019.

[30] L. Lan, L. Guoliang, and M. Shaobin, "Study on super-resolution reconstruction of single image based on convolution of sawtooth cavity residuals," *Journal of Xinjiang University (Natural Science Edition)(in English)*, vol. 38, no. 2, pp. 174–190, 2021.

[31] X. Shengjun, O. Puyan, G. Xueyuan, T. M. Khan, and D. Zhongxing, "Building segmentation in remote sensing image based on multiscale-feature fusion dilated convolution resnet," *Precision Engineering*, vol. 28, no. 7, pp. 1588–1599, 2020.

[32] H. Ran, Z. Guangmiao, and W. Rongjie, "Image de-rain algorithm based on residual block network," *Journal of Instrumentation*, vol. 41, no. 8, pp. 175–182, 2021.

[33] L. Zhenzhe, W. Guitang, C. Jianqiang, and F. Q. Shen, "A benign and malignant classification model of lung CT image nodules based on deep learning of residual network," *Journal of Instrumentation*, vol. 41, no. 3, pp. 248–256, 2020.

[34] A.-L. Wang, X.-Y. Song, and Y.-S. Chen, "Super-resolution reconstruction of remote sensing images based on recursive residual networks," *Computer Engineering and Applications*, vol. 55, no. 3, pp. 191–195, 2019.

[35] Y. Cheng, H. Zheng, X. W. Chen, S. H. O. Lin, and M. W. Zhang, "Image super-resolution algorithm based on dense residual attention network," *Computer System Applications*, vol. 30, no. 1, pp. 135–140, 2021.

[36] Y. Ma, N. Yu, Z. Xie, and L. Fenglin, "Metal artifact correction for CT images based on residual coding and decoding network," *Journal of Instrumentation*, vol. 41, no. 8, pp. 160–169, 2020.

[37] Z. Yunfei, *Super-Resolution Reconstruction Algorithm Based on Residual Structure and Dense Connection, [Ph.D. Thesis]*, Xi'an University of Electronic Science and Technology, 2020.

[38] Y. Zifu and L. Xiang, "Multi-scale dense residual networks for single image super-resolution reconstruction," *Chinese Journal of Graphics*, vol. 24, no. 3, pp. 410–419, 2019.

[39] Q. Jiayu, *Research on Multi-Scale Subnetworks and Single-Image Super-Resolution Combined with a Priori Information, [Ph.D. Thesis]*, South China University of Technology, 2020.

[40] X. Wang, *A Super-Resolution Reconstruction Method for Remote Sensing Images Based on Multi-Scale Feature Adaptive Fusion Network, [Ph.D. Thesis]*, Hubei University of Technology, 2020.

[41] R. Hu, Z. Baiting, and J. Xiaofen, "Two-way multi-scale residual networks for image super-resolution reconstruction," *Journal of Qingdao University of Science and Technology (Natural Science Edition)*, vol. 42, no. 3, pp. 107–118, 2021.

[42] Q. Huynh-Thu and M. Ghanbari, "Scope of validity of PSNR in image/video quality assessment," *Electronics Letters*, vol. 44, no. 13, pp. 800-801, 2008.

[43] Y. Wang, Y. Q. Wang, and X. H. Zhao, "A complex matrix structure similarity method for objective evaluation of image quality," *Journal of Instrumentation*, vol. 35, no. 5, pp. 1118–1129, 2014.

[44] Z. Wang, A. C. Bovik, H. R. Sheikh, and E. P. Simoncelli, "Image quality assessment: from error visibility to structural similarity," *IEEE Transactions on Image Processing*, vol. 13, no. 4, pp. 600–612, 2004.